iScience

CellPress
OPEN ACCESS

Article

Tumor cell-conditioned media drives collagen remodeling via fibroblast and pericyte activation in an *in vitro* premetastatic niche model

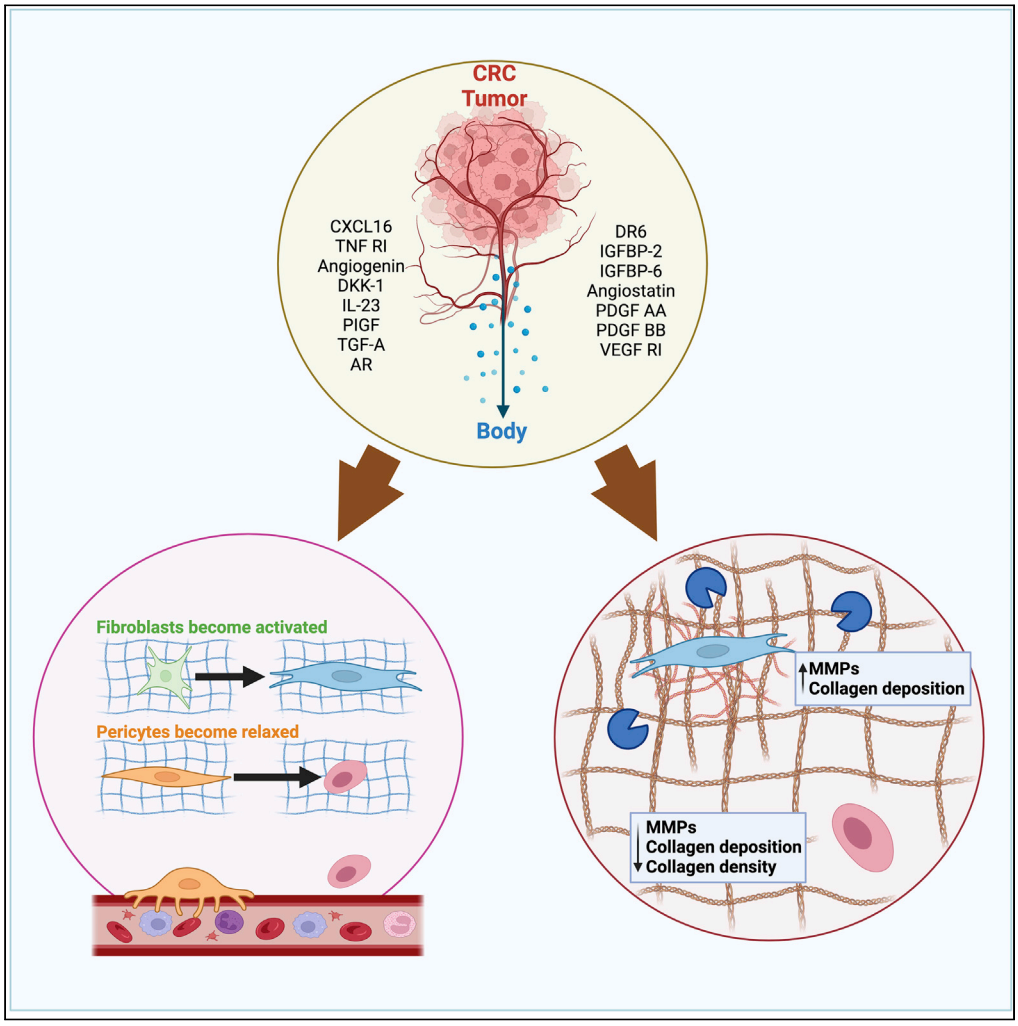

Kylie G. Nairon, Thomas J. DePalma, Joshua M. Zent, Jennifer L. Leight, Aleksander Skardal

skardal.1@osu.edu

Highlights

Colorectal cancer secreted factors (CCSFs) change cell behavior in distant tissues

CCSFs from metastatic cells activate myofibroblasts and cause pericyte relaxation

CCSF-treated fibroblasts increase matrix enzyme expression and collagen deposition

Pericytes exposed to CCSFs decrease matrix enzyme expression and collagen synthesis

Nairon et al., iScience 25, 104645
July 15, 2022
https://doi.org/10.1016/j.isci.2022.104645

iScience

CellPress
OPEN ACCESS

Article

Tumor cell-conditioned media drives collagen remodeling via fibroblast and pericyte activation in an *in vitro* premetastatic niche model

Kylie G. Nairon,[1] Thomas J. DePalma,[1] Joshua M. Zent,[1] Jennifer L. Leight,[1,2,3] and Aleksander Skardal[1,2,3,4,*]

SUMMARY

Primary tumors secrete large quantities of cytokines and exosomes into the bloodstream, which are uptaken at downstream sites and induce a pro-fibrotic, pro-inflammatory premetastatic niche. Niche development is associated with later increased metastatic burden, but the cellular and matrix changes in the niche that facilitate metastasis are yet unknown. Furthermore, there is no current standard model to study this phenomenon. Here, biofabricated collagen and hyaluronic acid hydrogel models were employed to identify matrix changes elicited by pericytes and fibroblasts after exposure to colorectal cancer-secreted factors. Focusing on myofibroblast activation and collagen remodeling, we report fibroblast activation and pericyte stunting in response to tumor signaling. In addition, we characterize contributions of both cell types to matrix dysregulation via collagen degradation, deposition, and architectural remodeling. With these findings, we discuss potential impacts on tissue stiffening and vascular leakiness and suggest pathways of interest for future mechanistic studies of metastatic cell-premetastatic niche interactions.

INTRODUCTION

Cancer metastasis is responsible for the vast majority of cancer-related deaths and remains nearly impossible to treat despite decades of oncological research (Dillekas et al., 2019). Although cancer death rates have fallen 1.8% annually over the past two decades, treatment for metastasized cancers has seen little success (Howlader et al., 2019). In colorectal cancer (CRC), patients with localized disease have a 91% 5-year survival rate, which drops drastically to 14% upon the onset of distant metastases (Howlader et al., 2019). Major obstacles to treating this disease stage lie largely in its systemic nature, drug resistance, and the years – potentially decade – over which metastasized cells may lay dormant (Pan et al., 2017; Puig et al., 2018). Metastasis-preventing therapeutics could revolutionize patient prognosis across the field of oncology. However, the mechanisms which allow primary tumor cells to enter the bloodstream, survive circulation, extravasate, and proliferate in foreign tissues are still poorly understood. Within the past several years, studies have shown that factors such as cytokines and exosomes, which are secreted by primary tumors into the bloodstream can induce changes in distant tissues that begin to replicate pro-tumorigenic microenvironments (Costa-Silva et al., 2015; Feng et al., 2019; Shao et al., 2018). Known as the premetastatic niche (PMN), this collection of cellular, extracellular matrix (ECM), and immunoregulatory changes are believed to facilitate metastatic cell invasion and survival. Deeper understanding of how these changes arise and interact with disseminated tumor cells could elucidate novel targets for preventive therapeutics that decrease metastatic disease.

Previously, Erler et al. found that matrix-crosslinking enzyme lysyl oxidase mediated a PMN formation through recruitment of bone marrow-derived cells to healthy tissues (Erler et al., 2009). Later, Costa-Silva et al. employed a mouse model of pancreatic cancer to demonstrate that primary tumor exosomes induced fibrotic pathways and inflammation via Kupffer cells in the liver, which in turn was associated with future increased metastatic burden (Costa-Silva et al., 2015). Both of these findings suggest that changes to the extracellular matrix (ECM) physical structure and composition influence metastatic colonization. Dysregulated ECM plays a large role in establishing primary tumors through disrupting cell polarity, increasing apoptotic evasion, and promoting cellular migration, and thus consequently ECM dysregulation in healthy tissues could aid in the survival and proliferation of metastasizing cells (Halaoui and McCaffrey, 2015;

[1]Department of Biomedical Engineering, College of Engineering, The Ohio State University, Columbus, OH 43210, USA

[2]The Ohio State University and Arthur G. James Comprehensive Cancer Center, Columbus, OH 43210, USA

[3]Center for Cancer Engineering, The Ohio State University, Columbus, OH 43210, USA

[4]Lead contact

*Correspondence: skardal.1@osu.edu

https://doi.org/10.1016/j.isci.2022.104645

Keely, 2011; Walker et al., 2018). No current model has fully characterized the properties or development of the PMN ECM.

The major barrier preventing progress toward understanding factors that promote PMN formation and mechanistic relationships between these changes and metastasis is reliance on animal models and traditional 2D cell culture. Studying systemic disease in animal models is a formidable task further complicated with confounding variables and difficulty in human translation. Furthermore, studying a metastatic site before metastasis occurs is near impossible, as typically tracking of fluorescent or luminescent tumor cells is used to identify metastases, but after identification, it is too late. These sites are no longer pre-metastatic. In addition, if one were to monitor tumor cell tracking to attempt to locate a PMN, the number of tissue sites to monitor is heavy on time and equipment. The alternative, 2D cell culture, does not offer the complexity required to replicate the ECM itself, PMN initiation and formation, or metastatic invasion. Bioengineered microphysiological systems (MPS) including 3D hydrogel-based organoids and microfluidic devices can provide cell-cell, cell-matrix protein, and mechanotransducive signaling similar to that of native human tissue while increasing ease of monitoring and controlling desired variables (Devarasetty et al., 2020; Hapach et al., 2019; Sontheimer-Phelps et al., 2019). In this way, direct relationships between cells, soluble factors, and the ECM can be parsed in ways not feasible in animal or 2D models. Recent MPS models of angiogenic sprouting (Bai et al., 2021) and tumor-stroma interplay in intravasation (Truong et al., 2019), and tumor organoid-based drug screening (Qi et al., 2018) clearly show the possibilities of MPS models in both basic and translational research. Some early steps have already been taken to leverage these technologies toward a deeper understanding of the PMN; a 2019 study by Kim H. et al. followed macrophage-driven remodeling in a microfluidic model of immune cell infiltration and a later model by Kim J. et al. demonstrated exosome-driven liver sinusoidal endothelial cell activation and basement membrane remodeling that corresponded with increased circulating tumor cell adhesion to vessel walls (Kim et al., 2019, 2020). Although these results are exciting and demonstrate the power of *in vitro* MPS models, they do not address ECM remodeling by resident stromal cells beyond the basement membrane, leaving unclear the methods by which the PMN ECM may support tumor cell viability and proliferation after extravasation.

To further our understanding of matrix remodeling in the PMN and the role of primary tumor signaling in PMN development, we utilized a naturally-derived hydrogel matrix model consisting of photocrosslinkable collagen I and hyaluronic acid (Mazzocchi et al., 2019). This environment features integral cell adhesion sites and can be degraded by cell-secreted matrix enzymes, remodeled, or supplemented with new ECM, by stromal cells. In this study, we employed this hydrogel platform to identify the phenotypic changes in fibroblasts and pericytes after exposure to tumor cell secretions and the resulting collagen restructuring in their local microenvironment. As myofibroblast progenitor cell types, both fibroblasts and pericytes play major, yet distinct, roles in matrix remodeling and vascular integrity. In addition, experiments included a range of metastatic and nonmetastatic colorectal cancer cell lines to investigate how these manipulations relate to a primary tumor's aggressiveness. Herein, we present findings on pericyte and fibroblast activation, collagen reorganization, and ECM protein deposition in response to CRC-secreted factors (CCSFs). With these findings, we both propose targets for future mechanistic work and an *in vitro* platform in which to perform these studies.

RESULTS

Model creation and colorectal cancer-secreted cytokine profiling

To begin to evaluate the influence of tumor cell-secreted factors on distant stromal cell populations, we generated conditioned media from several CRC cancer cell lines. These conditioned media were analyzed by cytokine arrays and administered to 3D cultures of fibroblasts or pericytes (Figure 1A). Our initial steps were to characterize soluble factor profiles for each of the cell types included in this study, and to furthermore generate a 3D microenvironment to both support pericyte and fibroblast functions and allow matrix remodeling. Requirements for hydrogel matrix materials included cell-mediated degradation, intrinsic cellular attachment points, and a range of stiffnesses similar to that of human soft tissues. Previous work from our lab has shown that hydrogels formed from methacrylated collagen I and thiolated hyaluronic acid support function for a wide range of cell types, and varying collagen concentrations, or alternatively introducing additional crosslinkers, can be used to fine-tune hydrogel stiffnesses (Mazzocchi et al., 2019; Votanopoulos et al., 2020). For the purposes of this study, it was found that a 3:1 ratio of 6 mg/mL collagen I to 1 mg/mL hyaluronic acid (HA) created a soft hydrogel (~3.5 kPa) into which both suspended fibroblasts

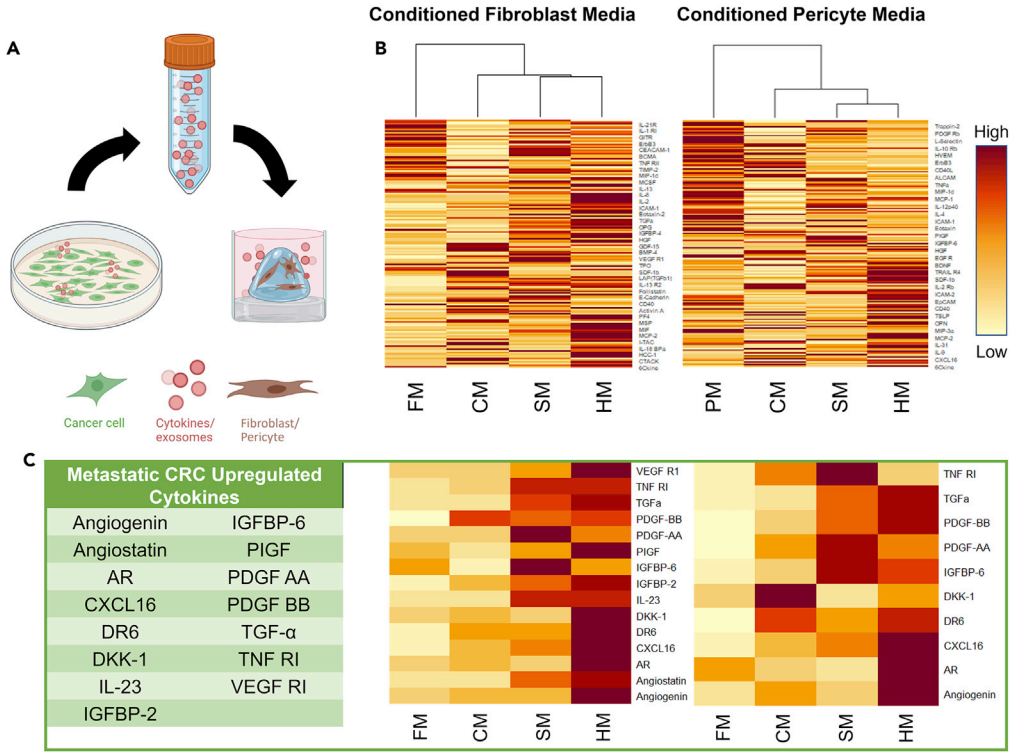

Figure 1. Model creation and colorectal cancer-secreted cytokine profiling

(A) Schematic of hydrogel model creation and cluster analysis of CRC cell line cytokine profiles. Media containing secreted cytokines and exosomes of Caco2, SW480, and HCT116 CRC cell lines was isolated via a centrifugation protocol. Normal human fibroblasts or microvascular pericytes were suspended in collagen I-hyaluronic acid hydrogel matrices and cultured in CRC conditioned media to study cellular response to primary tumor soluble signals.

(B–C) Clustering analysis of conditioned media based on a 200 cytokine array showed distinct signatures for conditioned media produced by each cell line.

Cytokines upregulated in metastatic cell-conditioned media and their expression levels are shown in (C). CM – Caco2 Media, SM – SW480 Media, HM – HCT116 Media, FM – Fibroblast Control Media, PM – Pericyte Control Media.

and pericytes attached and exhibited appropriate extended or spread-out morphologies. Matrix-tethered heparin, as a feature of the HA component, was included to increase cytokine and growth factor binding within the microenvironment (Bhakta et al., 2012).

To model the presence of a primary CRC tumor on pericytes and fibroblasts, we generated conditioned fibroblast or pericyte media from several CRC cell lines cultured for 24 h (Leibovitz et al., 1976; Rajput et al., 2008; Wang et al., 2015). To investigate the correlations between metastatic and nonmetastatic CRC types, a range of cell lines were chosen: Caco2 (a nonmetastatic CRC cell line), SW480, and HCT116 (both metastatic CRC cell lines, but with HCT116 considered more invasive). To account for media nutrient depletion during conditioning, control media was similarly conditioned for 24 h with either fibroblasts or pericytes. Quantitative cytokine profiles of the CCSFs as well as fibroblast and pericyte controls were determined with RayBiotech's cytokine array testing service. This 200 human cytokine panel included factors associated with immune recruitment, fibrosis, and angiogenesis, all crucial processes in tumor and metastasis development. Hierarchical clustering of cytokine expression levels indicated high degrees of uniqueness in each cell type, expected because of their variety of origins, functions, and phenotypes (Figure 1B). Cytokines that were consistently upregulated in metastatic (SW480 and HCT116) CRC lines relative to Caco2 or control samples are shown in Figure 1C. Full cytokine profiles with accompanying concentrations in media are shown in Tables S1–S5.

With this characterization of the secreted factors present in each condition, we suspended fibroblasts or pericytes in collagen I-HA hydrogels and cultured them in CCSF-containing or control media as diagrammed in Figure 1A.

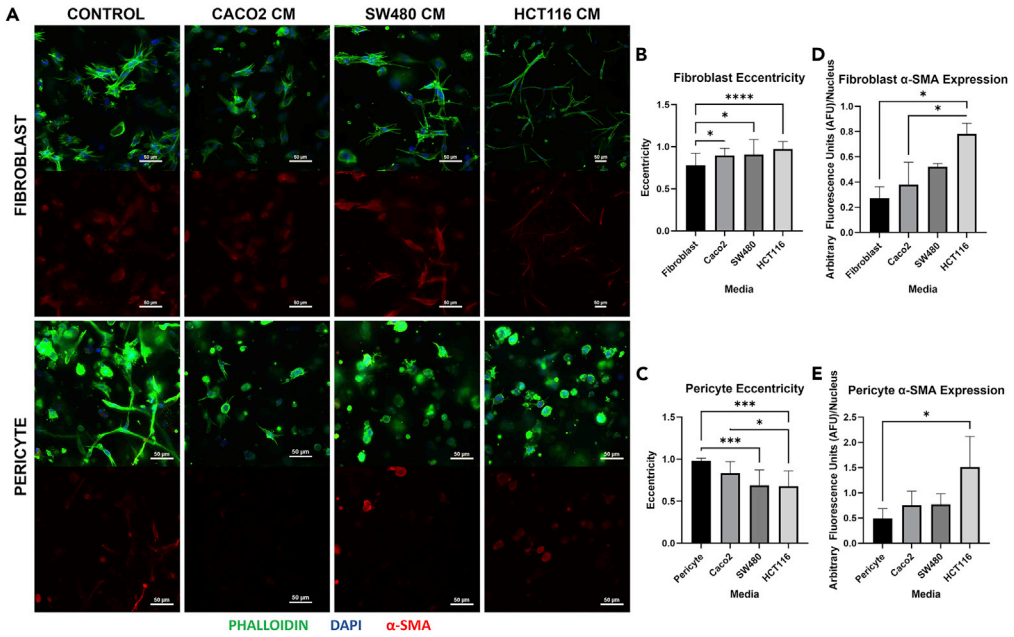

Figure 2. CRC Secretome Differentially Activates Pericytes and Fibroblasts in 3D Hydrogel Constructs. CRC-derived factors differentially activate fibroblasts and pericytes in the hydrogel microenvironment

(A) Representative images of phalloidin (green)/α-SMA (red)/DAPI (blue) stain on fibroblasts (top) and pericytes (bottom) treated for 3 days with colorectal cancer conditioned media.

(B and C) Eccentricity quantification of fibroblasts and pericytes in each condition, where a score of 0 indicates circularity, and a score nearing one indicates a spindle-like shape.

(D and E) Fluorescence quantification of α-SMA expression per cell. Scale bar 50 μm. Significance: *$p < 0.05$, ***$p < 0.001$, ****$p < 0.0001$. Data are represented as mean ± SEM.

CRC secretome differentially activates pericytes and fibroblasts in 3D hydrogel constructs

To study the effects of CCSFs on fibroblast and pericyte activation, we performed morphological analyses of both cell types in each condition after 3 days of hydrogel culture (Figure 2A). Phalloidin staining showed distinct differences in both pericytes and fibroblasts exposed to CCSFs, notably, HCT116 CM drives fibroblasts toward greater elongation and a spindle-like shape, while exposure to CCSFs from all CRC lines results in stunted, spherical pericyte phenotypes (Figures 2A and S1). To quantify these differences, eccentricity calculations were performed for all fully in-field cells (at least five cells per field of view) for $n \geq 3$ hydrogel constructs for each cell type. Using the eccentricity equation $b^2 = a^2(1 - e^2)$, where b is the semi-minor axis and a the semi-major axis of each cell, we measured the tendency of cells in each condition to elongate, or extend processes directionally. Following the qualitative findings in Figure 2A, fibroblasts cultured in conditioned media from all CRC cell types had a significantly greater $\boldsymbol{e}$ value than those grown in control conditions (Figure 2B). Inversely, HCT116 and SW480 CM significantly decreased pericyte eccentricity as compared to the control (Figure 2C). In addition, pericytes grown in the more aggressive HCT116 CM showed significantly lower eccentricity than those grown in the mild Caco2 CM, suggesting that highly metastatic primary tumor cells induce a greater phenotypic change in pericytes than mild, less invasive tumor cell types. Biologically, this is an important factor to note, as the function of pericytes relies on their ability to extend processes and wrap tightly around the microvasculature to maintain its structure and prevent excess leakiness or cellular transmigration of the endothelial barrier (Liu et al., 2021; Xian et al., 2006). Interrupting pericyte extension and contractility creates a vascular environment permissible to disseminated tumor cell extravasation, increasing the ease and likelihood of micrometastasis formation at downstream sites.

Following this morphological analysis, we stained fibroblasts and pericytes with alpha-smooth muscle actin (α-SMA) antibody, a common marker for myofibroblast activation that is often upregulated during fibrosis (Shinde et al., 2017; Yamaguchi et al., 2020). Fluorescence quantification showed an increased α-SMA expression for both pericytes and fibroblasts exposed to metastatic CRC conditioned media (Figures 2D

and 2E). HCT116 media induced significantly higher α-SMA expression as compared to control conditions for both cell types and as compared to Caco2 media for fibroblast cultures. It is well documented that extracellular matrix stiffness and collagen density are elevated in the primary tumor microenvironment, and that these properties also impact cancer cell motility and directional migration in primary sites (Jones et al., 2019; Provenzano et al., 2006). Activating fibroblasts in distant tissues toward creating a fibrotic matrix may similarly aid metastasizing cells in invading and colonizing secondary metastasis sites.

Pericytes exhibit a relaxed phenotype in response to CRC-secreted factors

The roles of pericyte behavior in the metastatic cascade are highly controversial in current research and largely uncharacterized. However, their importance in disease progression has become more widely recognized over the last decade (Paiva et al., 2018; Picoli et al., 2021). Current discussions of pericytes in cancer metastasis largely center on their role in angiogenesis (Chen et al., 2016; Taeger et al., 2011). Although a major topic in oncology, this neglects pericytes' additional functions in regulating vascular permeability via cell coverage and basement membrane maintenance, two functions of particular interest in metastatic extravasation. To further interrogate biological implications of the morphological changes observed upon CCSF treatment, we stained pericytes cultured for three days in CCSFs for phosphorylated myosin light chain (*p*-MLC) and paxillin.

Myosin light chains are important in cellular contractility and locomotion and are regulated via phosphorylation level. In pericytes specifically, decreases in *p*-MLC are associated with pericyte relaxation, resulting in gaps in microvessel coverage (Pellowe et al., 2018; Wang et al., 2012). Fluorescent staining for myosin light chain in pericytes showed that pericytes cultured in CCSFs had decreased phosphorylation levels relative to the pericyte CM control (Figure 3A(iii)). Further quantification of cellular *p*-MLC across multiple samples and regions of interest showed a significant decrease in phosphorylation for pericytes cultured in HCT116 CM as compared to the pericyte CM control (Figure 3B). Combined, our observations of decreased cellular extension and low myosin light chain phosphorylation are indicative of a relaxed pericyte phenotype that, biologically, corresponds with low pericyte vessel coverage. These destabilized, low coverage vessels have been shown in prior work to lead to increased tumor cell extravasation and metastatic invasion (He et al., 2020; Yonenaga et al., 2005). Staining for paxillin, a protein expressed at focal adhesions and a major player in cytoskeleton-matrix interactions, showed no quantifiable difference in expression across all pericyte conditions (Figure 3C). However, we noticed a shift from even paxillin distribution across the cell body in control and Caco2 CM pericytes to more sparse, punctate staining in the higher grade SW480 and HCT116 CM conditions (Figure 3A(iv)). This seems to indicate changes in pericyte cytoskeleton-ECM interactions in response to soluble signals from metastatic CRC cells. While this is an interesting finding, we plan to further investigate the mechanisms behind these changes and their implications in vascular structure in future studies.

CRC secretome drives matrix metalloproteinase signaling and collagen deposition

We next investigated if these activation state changes resulted in increased or decreased collagen remodeling in the local microenvironment. Matrix metalloproteinases (MMPs) are a family of enzymes capable of degrading ECM proteins, especially collagens, and modulating cell adhesion and migration through the ECM. MMPs 2 and 9, specifically, can degrade collagen IV, a major component of the basement membrane. Along with MMP-13, these MMPs are associated with CRC metastasis and general tissue remodeling (Araújo et al., 2015; Yamada et al., 2010). To assess MMP expression in our hydrogel model during CCSF exposure, we ran quantitative ELISAs on days 2 and 4 to measure MMP2, 9, and 13 expressions over these periods of remodeling. As the results from each 48 h period are similar, only analysis of the second dataset (48–96h) is shown in Figure 4 for concision. Aligning with activation state changes observed in Figure 2, both MMP2 and MMP9 expression by fibroblasts was significantly upregulated when cultured with SW480 conditioned media, whereas all other CCSFs showed no impact (Figures 4A and 4B). However, fibroblast MMP13 expression increased in response to all types of CCSFs, with the greatest increase in HCT116 conditioned media (Figure 4C). Pericyte MMP activity similarly corresponds with decreased activation, with MMP2 expression dropping significantly for all CCSF types as compared to the pericyte control, and additionally for HCT116 conditioned media culture as compared to Caco2 CCSFs (Figure 4D). MMP9 was interestingly upregulated for SW480 conditions alone, and pericyte MMP13 expression did not show any major trends in relation to media type (Figures 4E and 4F). As a global measure of pan-MMP activity in our hydrogel model during CCSF culture, we employed a previously developed MMP-cleavable biosensor peptide into the Col-HA matrix via thiol-thiol and thiol-methacrylate linkages

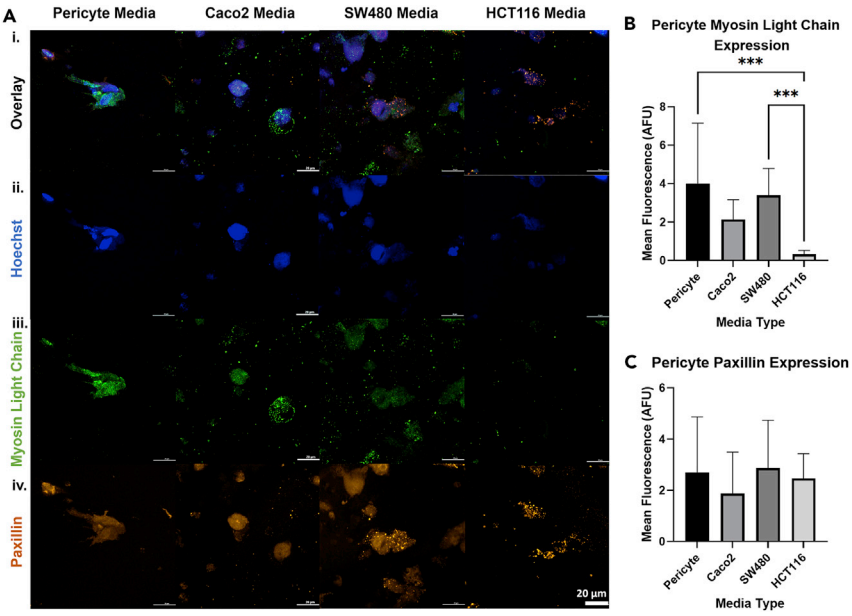

Figure 3. Pericytes Exhibit a Relaxed Phenotype in Response to CRC-Secreted Factors

CRC-derived factors promote pericyte relaxation and changes in cell-matrix interactions. (an i-iv) Representative images of pericytes stained for phosphorylated myosin light chain (green, iii.), paxillin (orange, iv.), and cell nuclei (blue, ii.) after three days of culture in conditioned media.

(B) Fluorescence quantification of *p*-MLC. Phosphorylation of myosin light chain decreases significantly in pericytes exposed to HCT116 CM as compared to control conditions.

(C) Fluorescence quantification of paxillin. No significant change in paxillin expression was observed for any condition, despite visual differences in staining patterns. Scale bar 20 μm. Significance: ***$p < 0.001$. Data are represented as mean ± SEM

(Figure S2A). Fluorescence measurements on Day 4 of culture showed increased MMP activity for all fibroblast hydrogels cultured in CCSF media relative to control and decreased MMP activity for pericyte CCSF cultures (Figure S2B).

After examining matrix degradation, we then investigated matrix deposition. While many proteins and polysaccharides are at play during this process, we focused on fibrillar collagens as the most abundant component of the ECM. Fibrillar collagens are secreted in an immature form and are later crosslinked extracellularly to form stable fibrils. Until this maturation, which takes place over several days, the novel collagen remains acid soluble, and can thus be distinguished from mature, preexisting collagen. Using the Sircol colorimetric assay, we isolated this newly deposited collagen from pericyte and fibroblast hydrogel constructs after four days of culture in CCSFs. Additional measurements at day 0 and day 2 are provided in Figure S3. Interestingly, for fibroblasts, collagen deposition was upregulated only when cultured in HCT116 conditioned media; no other CRC secreted factors resulted in a change in collagen deposition relative to the control (Figure 4G). For pericytes, there was no significant difference for any condition as compared to the normal control (Figure 4H).

Pericytes and fibroblasts reorganize collagen fiber architecture and density in the presence of CCSFs

We finally examined collagen architectural changes in the fibroblast and pericyte microenvironments in response to CCSFs. Picrosirius red staining of histological sections combined with polarized light microscopy was used to visually extract collagen fibers from the overall hydrogel matrix (Figure 5A). In this stain, red/orange colors appear for thicker, more mature collagen fibers, while yellow/green colors indicate thinner, less mature fibers. Visual inspection of the samples showed a higher proportion of yellow and green, or thinner collagen fibers, in both fibroblast and pericyte cultures exposed to Caco2 conditioned media. In addition, there was an obvious decrease in collagen fiber density for pericyte hydrogels cultured

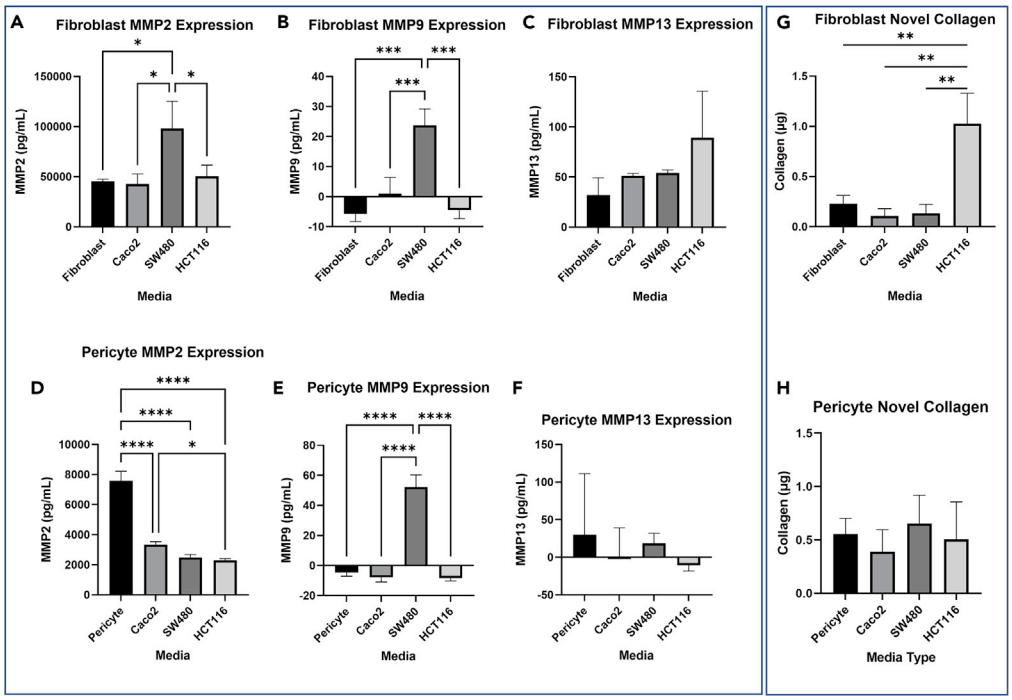

Figure 4. CRC Secretome Drives Matrix Metalloproteinase Signaling and Collagen Deposition

CCSF exposure changes collagen degradation and deposition behaviors for both pericytes and fibroblasts.

(A–C) SW480 conditioned media significantly increases MMPs two and nine expressions by fibroblasts. All CRC media upregulate MMP13 expression, with HCT116 media inducing the largest change.

(D–F) Pericyte MMP2 expression is significantly downregulated with exposure to CCSFs, and additionally correlates with CRC cell line aggression.

Pericyte MMP13 is underexpressed with CCSF exposure, and MMP9 shows no clear trend relative to media type.

(G and H) HCT116 conditioned media significantly increases the quantity of collagen deposition by fibroblasts; pericytes follow the same trend but have no significant changes. Significance: *$p < 0.05$, **$p < 0.01$, ***$p < 0.001$, ****$p < 0.0001$. Data are represented as mean ± SEM $n \geq 3$.

in metastatic CRC conditioned media as compared to nonmetastatic or control conditions. CT-FIRE quantification of imaged collagen fibers reflected this observation, with pericyte-derived collagen fiber density significantly reduced in SW480 and HCT116 conditioned media (Figure 5B). For fibroblasts, there was a slight increase in density for all CCSF conditions, but no significant changes. Fiber width and length varied but did not correlate with tumor/nontumor conditions for fibroblasts or pericytes. Fiber alignment distribution was wider for fibroblasts and pericytes cultured in HCT116 CCSFs as compared control, indicating a less aligned, more disorganized matrix (Figure 5C). Overlays of the CT-Fire extracted fibers over the original grayscale images for each sample are shown in Figure S4.

DISCUSSION

Metastasis remains an incurable disease and the primary cause of cancer-related deaths, despite major improvements in treatments for primary tumors. Distant lesions can be drug-resistant, hard to detect, and may lay dormant for years, resulting in significant challenges to treat them effectively. Preventative interventions against metastatic colonization could immensely improve patient prognosis and quality of life, but research has not yet provided a clear understanding of many of the mechanisms that drive or enable metastatic events to occur. It has been shown that primary tumors communicate with distant tissues via secreted factors and can alter the behaviors of native cells, which in turn correlates with increased metastatic burden in animal models. Unfortunately, the underlying factors connecting these two phenomena have not been fully described. Understanding the cellular and microenvironmental changes primary tumors elicit in potential metastatic sites and the mechanisms by which these changes occur could bring oncological research one step closer to the ability to target and prevent metastatic growth.

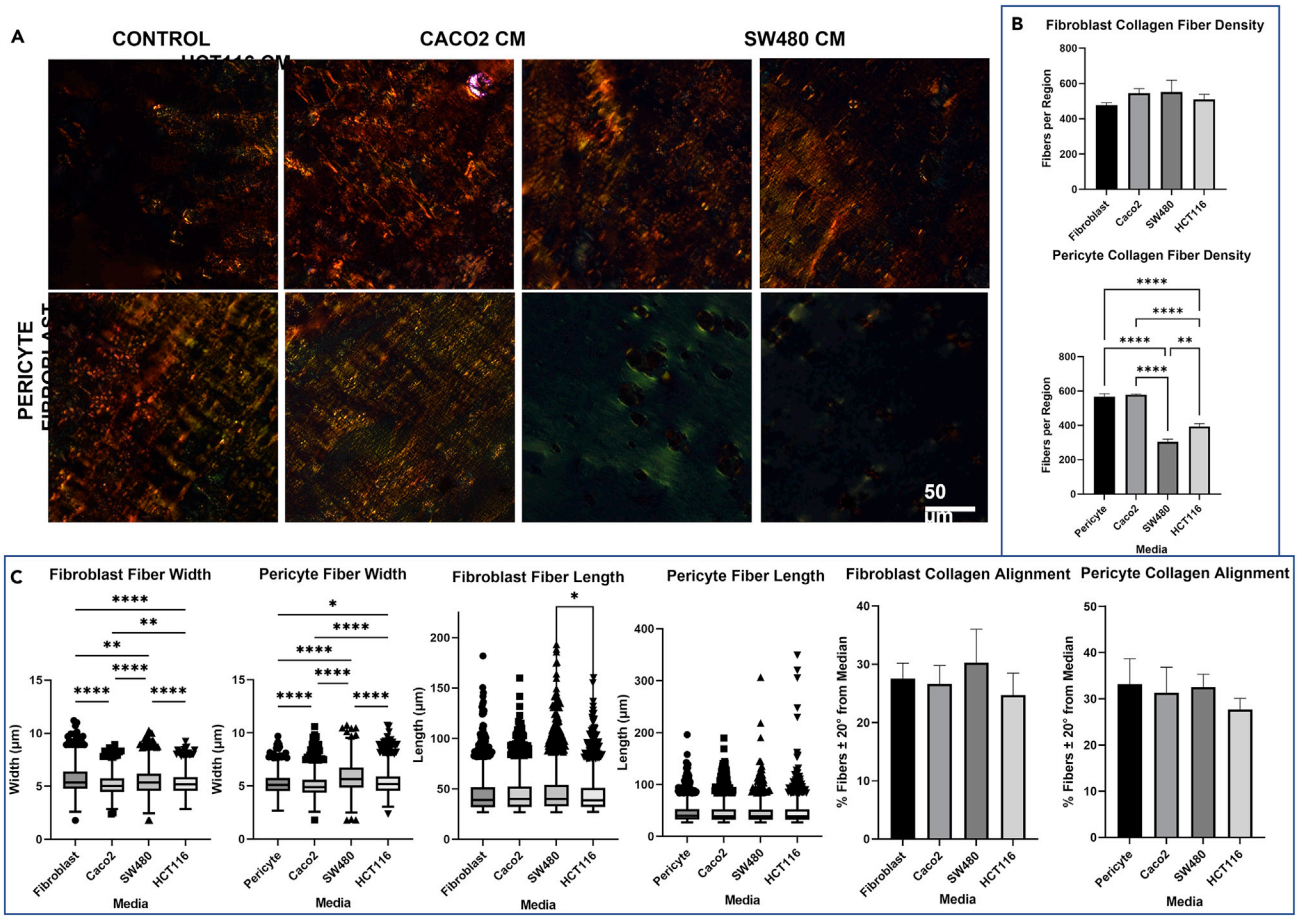

Figure 5. Pericytes and Fibroblasts Reorganize Collagen Fiber Architecture and Density in the Presence of CCSFs

Picrosirius red stain of collagen fibers in fibroblast and pericyte-laden hydrogels.

(A) Polarized light images of picrosirius red stains were analyzed using CT-Fire software.

(B) Collagen fiber density was slightly increased for all CCSF conditions in fibroblast cultures, and significantly lowered for SW480 and HCT116 conditions in pericyte cultures.

(C) Collagen fiber width skewed lower in fibroblasts CCSF cultures compared to normal control and higher in pericyte SW480 and HCT116 cultures. Fiber length was not affected by CCSF exposure in either fibroblast or pericyte cultures. Collagen alignment was lower, i.e., was less organized, in fibroblast and pericyte hydrogels cultured with HCT116 media. Scale bar 50 μm. Significance: *$p < 0.05$, **$p < 0.01$, ***$p < 0.001$, ****$p < 0.0001$. Bar plots are shown as mean ± SEM Box and whisker plots are presented with Tukey formatting and horizontal bar at the median.

In this work, we employed hyaluronic acid and collagen ECM hydrogel constructs, containing either fibroblasts or pericytes, that were treated with conditioned media from three commonly used colorectal cancer cell lines of varying levels of metastatic potential to begin to obtain a glimpse at how tumor-secreted factors could influence downstream cells in other tissues. Specifically, we evaluated the impact of these tumor-secreted factors on fibroblast and pericyte morphology, α-SMA and paxillin expression, myosin light chain phosphorylation, collagen deposition and architecture, and MMP expression.

Through initial cytokine array assays, we saw that each of these conditioned media had distinct cytokine profiles, with a number of potent cytokines increasing in the conditioned media obtained from the more invasive tumor cells. We then detailed important changes in pericyte and fibroblast-derived tissue remodeling in response to these soluble signals secreted by the CRC cells. Despite the fact that both fibroblasts and pericytes are myofibroblast progenitors, they vary greatly in signaling response, which may point toward important functional mechanisms in regulating the perivascular premetastatic microenvironment. Morphologically, fibroblasts become more spindle-shaped in response to CCSFs, and α-SMA expression increases, indicative of a more activated myofibroblast phenotype. Correspondingly, CCSF-treated fibroblasts increased both collagen degradation, via MMPs, and novel collagen deposition. Although changes

to the greater collagen architecture were modest, CCSF exposure led fibroblasts to create a slightly more disorganized matrix in comparison to the normal conditions observed in our hydrogel constructs. Pericytes, on the other hand, were unable to extend processes into their surrounding matrix when exposed to CCSFs. Further analysis revealed that CCSFs induced a relaxed phenotype in pericytes, associated with low vessel coverage. CCSFs largely inhibited pericytes from degrading or depositing collagen, leading to decreased collagen density within the microenvironment relative to that of normal culture conditions. Importantly, the greatest changes for both fibroblasts and pericytes were only observed with signaling from one or both of the metastatic CRC cell lines (SW480 and HCT116), and not from a nonmetastatic CRC line (Caco2), indicating that these behavioral and matrix changes are not only a response to the presence of a primary tumor, but are specifically induced by tumor cells capable of metastasis.

These localized changes directly relate to the ability to prepare these niche ECMs to primary tumors that are able to complete the metastatic cascade. Physiologically, reducing pericyte contractility around microvasculature and impairing basement membrane deposition and repair could result in dysregulated, leaky vasculature that simplifies extravasation for circulating tumor cells. We will test this hypothesis in a future set of studies by incorporating an endothelial cell layer into the model to study pericyte-endothelial disruptions in the presence of CCSFs. Likewise, a stiff, fibrotic matrix produced by activated fibroblast more closely resembles the primary tumor ECM, promoting metastasizing cell engraftment, survival, and colonization in unfamiliar tissues. With the findings from this study and development of the model herein, we can expand to study tissue-specific premetastatic remodeling in the liver (Mazzocchi et al., 2019; Skardal et al., 2015) and lung (Aleman and Skardal, 2018; Skardal et al., 2017). In our existing metastasis-on-a-chip (MOC) model, we have observed spontaneous dissemination of primary tumor cells and tissue-specific invasion into downstream liver and lung hydrogel constructs (Aleman and Skardal, 2018). Applying the results from this work to such a model could allow us to dig deeper into the mechanisms behind this organotropic specificity. Although these are early findings, both of the separate responses of pericytes and fibroblasts to the primary tumor secretome could potentially work together to prepare a hospitable site for metastatic colonization and growth.

In the future, we aim to combine the concept of a hydrogel premetastatic niche with our MOC, paired with pathway specific studies, genomic sequencing of cells that metastasize versus those that do not, and even patient-specific diagnostics. With personalized medicine leading and informing the next generation of clinical practice, the ability to predict individual patients' metastatic patterns or potential for metastasis based on premetastatic changes could be an invaluable prognostic tool.

Limitations of the study

There are extraordinarily few existing models of the premetastatic niche, a phenomenon which is nearly impossible to study in animals and even more so in traditional cell culture. These findings show the potential of 3D models to ask specific questions about premetastatic niche characteristics and formation to fill this gap. However, these are initial findings, and future iterations, such as those described above using our MOC platform, must be made to address the study's limitations. Perhaps most importantly, this model lacks the ability to track metastasized cells' interactions with the modified hydrogel niches and link these interactions back to specific mechanisms. In addition, the model is limited by its lack of biomimetic spatial structure, such as endothelial cell-lined vasculature to allow pericyte wrapping and cell-cell interactions. However, ongoing work in our laboratory aims to generate endothelialized barriers within our tumor-on-a-chip devices to more accurately model the entire metastatic cascade. In addition, in this study, we focused on tumor cell secreted factors in the form of cytokines and growth factors. We did not evaluate the conditioned media in the context of mRNAs and exosomes. We hope to begin to assess these types of tumor cell secreted factors in future studies as well.

STAR★METHODS

Detailed methods are provided in the online version of this paper and include the following:

- KEY RESOURCES TABLE
- RESOURCE AVAILABILITY
  - Lead contact
  - Materials availability
  - Data and code availability

SUPPLEMENTAL INFORMATION

Supplemental information can be found online at https://doi.org/10.1016/j.isci.2022.104645.

ACKNOWLEDGMENTS

A.S. and J.L. acknowledge funding through the Ohio State University Comprehensive Cancer Center and the Pelotonia foundation. A.S. acknowledges funding from NIH grant R21CA229027. KN acknowledges resources from the Campus Microscopy and Imaging Facility (CMIF) and the OSU Comprehensive Cancer Center (OSUCCC) Microscopy Shared Resource (MSR), The Ohio State University through NIH grant P30CA016058.

AUTHOR CONTRIBUTIONS

Conceptualization, K.N. and A.S.; Methodology, K.N., J.Z., and A.S.; Investigation, K.N. and T.D.; Resources, J.Z. and J.L.; Writing – Original Draft, K.N. and A.S.; Writing – Review & Editing, A.S., J.L., T.D., and K.N.; Supervision, A.S.; Funding Acquisition, A.S.

DECLARATION OF INTERESTS

The authors declare no competing interests.

INCLUSION AND DIVERSITY

We worked to ensure diversity in experimental samples through the selection of the cell lines. One or more of the authors of this paper self-identifies as a member of the LGBTQ + community. While citing references scientifically relevant for this work, we also actively worked to promote gender balance in our reference list.

Received: December 9, 2021
Revised: May 25, 2022
Accepted: June 15, 2022
Published: July 15, 2022

REFERENCES

Aleman, J., and Skardal, A. (2018). A multi-site metastasis-on-a-chip microphysiological system for assessing metastatic preference of cancer cells. Biotechnol. Bioeng. *116*, 936–944. https://doi.org/10.1002/bit.26871.

Araújo Jr, R., Lira, G.A., Vilaça, J., Guedes, H.G., Leitão, M., Lucena, H.F., and Ramos, C.C.O. (2015). Prognostic and diagnostic implications of MMP-2, MMP-9, and VEGF-α expressions in colorectal cancer. Pathol. Res. Pract. *211*, 71–77. https://doi.org/10.1016/j.prp.2014.09.007.

Bai, J., Khajavi, M., Sui, L., Fu, H., Tarakkad Krishnaji, S., Birsner, A.E., Bazinet, L., Kamm, R., and D'Amato, R.J. (2021). Angiogenic responses in a 3D micro-engineered environment of primary endothelial cells and pericytes. Angiogenesis *24*, 111–127. https://doi.org/10.1007/s10456-020-09746-6.

Bhakta, G., Rai, B., Lim, Z.X., Hui, J.H., Stein, G.S., van Wijnen, A.J., Nurcombe, V., Prestwich, G.D., and Cool, S.M. (2012). Hyaluronic acid-based hydrogels functionalized with heparin that support controlled release of bioactive BMP-2. Biomaterials *33*, 6113–6122. https://doi.org/10.1016/j.biomaterials.2012.05.030.

Bredfeldt, J.S., Liu, Y., Conklin, M.W., Keely, P.J., Mackie, T.R., and Eliceiri, K.W. (2014a). Automated quantification of aligned collagen for human breast carcinoma prognosis. J. Pathol. Inf. *5*, 28. https://doi.org/10.4103/2153-3539.139707.

Bredfeldt, J.S., Liu, Y., Pehlke, C.A., Conklin, M.W., Szulczewski, J.M., Inman, D.R., Keely, P.J., Nowak, R.D., Mackie, T.R., and Eliceiri, K.W.

(2014b). Computational segmentation of collagen fibers from second-harmonic generation images of breast cancer. J. Biomed. Opt. *19*, 016007. https://doi.org/10.1117/1.jbo.19.1.016007.

Chen, Z., Xu, X., and Hu, J. (2016). Role of pericytes in angiogenesis: focus on cancer angiogenesis and anti-angiogenic therapy. Neoplasma *63*, 173–182. https://doi.org/10.4149/201_150704n369.

Costa-Silva, B., Aiello, N.M., Ocean, A.J., Singh, S., Zhang, H., Thakur, B.K., Becker, A., Hoshino, A., Mark, M.T., Molina, H., et al. (2015). Pancreatic cancer exosomes initiate pre-metastatic niche formation in the liver. Nat. Cell Biol. *17*, 816–826. https://doi.org/10.1038/ncb3169.

Devarasetty, M., Dominijanni, A., Herberg, S., Shelkey, E., Skardal, A., and Soker, S. (2020). Simulating the human colorectal cancer microenvironment in 3D tumor-stroma co-cultures *in vitro* and *in vivo*. Sci. Rep. *10*, 9832. https://doi.org/10.1038/s41598-020-66785-1.

Dillekås, H., Rogers, M., and Straume, O. (2019). Are 90% of deaths from cancer caused by metastases? Cancer Med. *8*, 5574–5576. https://doi.org/10.1002/cam4.2474.

Erler, J.T., Bennewith, K.L., Cox, T.R., Lang, G., Bird, D., Koong, A., Le, Q.-T., and Giaccia, A.J. (2009). Hypoxia-induced lysyl oxidase is a critical mediator of bone marrow cell recruitment to form the premetastatic niche. Cancer Cell *15*, 35–44. https://doi.org/10.1016/j.ccr.2008.11.012.

Feng, W., Dean, D.C., Hornicek, F.J., Shi, H., and Duan, Z. (2019). Exosomes promote pre-metastatic niche formation in ovarian cancer. Mol. Cancer *18*, 124. https://doi.org/10.1186/s12943-019-1049-4.

Halaoui, R., and McCaffrey, L. (2015). Rewiring cell polarity signaling in cancer. Oncogene *34*, 939–950. https://doi.org/10.1038/onc.2014.59.

Hapach, L.A., Mosier, J.A., Wang, W., and Reinhart-King, C.A. (2019). Engineered models to parse apart the metastatic cascade. NPJ Precis. Oncol. *3*, 20. https://doi.org/10.1038/s41698-019-0092-3.

He, Q., Li, X., He, L., Li, Y., Betsholtz, C., and Welsh, M. (2020). Pericyte dysfunction due to Shb gene deficiency increases B16F10 melanoma lung metastasis. Int. J. Cancer *147*, 2634–2644. https://doi.org/10.1002/ijc.33110.

Howlader, N., Noone, A., Krapcho, M., Miller, D., Brest, A., Yu, M., Ruhl, J., Tatalovich, Z., Mariotto, A., Lewis, D., et al. (2019). In SEER Cancer Statistics Review (N.C. Institute), pp. 1975–2017.

Jones, C.E., Hammer, A.M., Cho, Y., Sizemore, G.M., Cukierman, E., Yee, L.D., Ghadiali, S.N., Ostrowski, M.C., and Leight, J.L. (2019). Stromal PTEN regulates extracellular matrix organization in the mammary gland. Neoplasia *21*, 132–145. https://doi.org/10.1016/j.neo.2018.10.010.

Keely, P.J. (2011). Mechanisms by which the extracellular matrix and integrin signaling act to regulate the switch between tumor suppression and tumor promotion. J. Mammary Gland Biol. Neoplasia *16*, 219. https://doi.org/10.1007/s10911-011-9226-0.

Kim, H., Chung, H., Kim, J., Choi, D.-H., Shin, Y., Kang, Y.-G., Kim, B.-M., Seo, S.-U., Chung, S., and Seok, S.-H. (2019). Macrophages-triggered sequential remodeling of endothelium-interstitial matrix to form pre-metastatic niche in microfluidic tumor microenvironment. Adv. Sci. *6*, 1900195. https://doi.org/10.1002/advs.201900195.

Kim, J., Lee, C., Kim, I., Ro, J., Kim, J., Min, Y., Park, J., Sunkara, V., Park, Y.-S., Michael, I., et al. (2020). Three-dimensional human liver-chip emulating premetastatic niche formation by breast cancer-derived extracellular vesicles. ACS Nano *14*, 14971–14988. https://doi.org/10.1021/acsnano.0c04778.

Leibovitz, A., Stinson, J.C., McCoy, C., Mazur, K., and Mabry, N. (1976). Classification of human colorectal adenocarcinoma cell lines. Cancer Res. *36*, 4562–4569.

Leight, J.L., Alge, D.L., Maier, A.J., and Anseth, K.S. (2013). Direct measurement of matrix metalloproteinase activity in 3D cellular microenvironments using a fluorogenic peptide substrate. Biomaterials *34*, 7344–7352. https://doi.org/10.1016/j.biomaterials.2013.06.023.

Liu, Y., Zhang, H., Wang, S., Guo, Y., Fang, X., Zheng, B., Gao, W., Yu, H., Chen, Z., Roman, R.J., and Fan, F. (2021). Reduced pericyte and tight junction coverage in old diabetic rats are associated with hyperglycemia-induced cerebrovascular pericyte dysfunction. Am. J. Physiol. Heart Circ. Physiol. *320*, H549–H562. https://doi.org/10.1152/ajpheart.00726.2020.

Mazzocchi, A., Devarasetty, M., Huntwork, R., Soker, S., and Skardal, A. (2019). Optimization of collagen type I-hyaluronan hybrid bioink for 3D bioprinted liver microenvironments. Biofabrication *11*, 015003. https://doi.org/10.1088/1758-5090/aae543.

Paiva, A.E., Lousado, L., Guerra, D., Azevedo, P.O., Azevedo, P., Sena, I.F., Sena, I., Andreotti, J.P., Andreotti, J., Santos, G.S., et al. (2018). Pericytes in the premetastatic niche. Cancer Res. *78*, 2779–2786. https://doi.org/10.1158/0008-5472.can-17-3883.

Pan, H., Gray, R., Braybrooke, J., Davies, C., Taylor, C., McGale, P., Peto, R., Pritchard, K.I., Bergh, J., Dowsett, M., and Hayes, D.F. (2017). 20-Year risks of breast-cancer recurrence after stopping endocrine therapy at 5 Years. N. Engl. J. Med. *377*, 1836–1846. https://doi.org/10.1056/nejmoa1701830.

Pellowe, A., Sauler, M., Hou, Y., Merola, J., Liu, R., Calderon, B., Lauridsen, H.M., Lauridsen, H., Harris, M.R., Harris, M., et al. (2018). Endothelial cell-secreted MIF reduces pericyte contractility and enhances neutrophil extravasation. FASEB J. *33*, 2171–2186. https://doi.org/10.1096/fj.201800480r.

Picoli, C.C., Gonçalves, B.Ô., Santos, G.S., Rocha, B.G., Costa, A.C., Resende, R.R., and Birbrair, A. (2021). Pericytes cross-talks within the tumor microenvironment. Biochim. Biophys. Acta Rev. Canc *1876*, 188608. https://doi.org/10.1016/j.bbcan.2021.188608.

Provenzano, P.P., Eliceiri, K.W., Campbell, J.M., Inman, D.R., White, J.G., and Keely, P.J. (2006). Collagen reorganization at the tumor-stromal interface facilitates local invasion. BMC Med. *4*, 38. https://doi.org/10.1186/1741-7015-4-38.

Puig, I., Tenbaum, S.P., Chicote, I., Arqués, O., Martínez-Quintanilla, J., Cuesta-Borrás, E., Ramírez, L., Gonzalo, P., Soto, A., Aguilar, S., et al. (2018). TET2 controls chemoresistant slow-cycling cancer cell survival and tumor recurrence. J. Clin. Investig. *128*, 3887–3905. https://doi.org/10.1172/jci96393.

Sun, Q., Tan, S.H., Chen, Q., Ran, R., Hui, Y., Chen, D., and Zhao, C.-X. (2018). Microfluidic formation of coculture tumor spheroids with stromal cells as a novel 3D tumor model for drug testing. ACS Biomater. Sci. Eng. *4*, 4425–4433. https://doi.org/10.1021/acsbiomaterials.8b00904.

Rajput, A., Dominguez San Martin, I., Rose, R., Beko, A., LeVea, C., Sharratt, E., Mazurchuk, R., Hoffman, R.M., Brattain, M.G., and Wang, J. (2008). Characterization of HCT116 human colon cancer cells in an orthotopic model. J. Surg. Res. *147*, 276–281. https://doi.org/10.1016/j.jss.2007.04.021.

RStudio Team. RStudio: Integrated Development for R. RStudio, PBC. http://www.rstudio.com/.

Schneider, C.A., Rasband, W.S., and Eliceiri, K.W. (2012). NIH Image to ImageJ: 25 years of image analysis. Nat. Methods *9*, 671–675. https://doi.org/10.1038/nmeth.2089.

Shao, Y., Chen, T., Zheng, X., Yang, S., Xu, K., Chen, X., Xu, F., Wang, L., Shen, Y., Wang, T., et al. (2018). Colorectal cancer-derived small extracellular vesicles establish an inflammatory premetastatic niche in liver metastasis. Carcinogenesis *39*, 1368–1379. https://doi.org/10.1093/carcin/bgy115.

Shinde, A.V., Humeres, C., and Frangogiannis, N.G. (2017). The role of α-smooth muscle actin in fibroblast-mediated matrix contraction and remodeling. Biochim. Biophys. Acta Mol. Basis Dis. *1863*, 298–309. https://doi.org/10.1016/j.bbadis.2016.11.006.

Skardal, A., Devarasetty, M., Soker, S., and Hall, A.R. (2015). *In situ* patterned micro 3D liver constructs for parallel toxicology testing in a fluidic device. Biofabrication *7*, 031001. https://doi.org/10.1088/1758-5090/7/3/031001.

Skardal, A., Murphy, S.V., Devarasetty, M., Mead, I., Kang, H.-W., Seol, Y.-J., Shrike Zhang, Y., Shin, S.-R., Zhao, L., Aleman, J., et al. (2017). Multi-tissue interactions in an integrated three-tissue organ-on-a-chip platform. Sci. Rep. *7*, 8837. https://doi.org/10.1038/s41598-017-08879-x.

Sontheimer-Phelps, A., Hassell, B.A., and Ingber, D.E. (2019). Modelling cancer in microfluidic human organs-on-chips. Nat. Rev. Cancer *19*, 65–81. https://doi.org/10.1038/s41568-018-0104-6.

Taeger, J., Moser, C., Hellerbrand, C., Mycielska, M.E., Glockzin, G., Schlitt, H.J., Geissler, E.K., Stoeltzing, O., and Lang, S.A. (2011). Targeting FGFR/PDGFR/VEGFR impairs tumor growth, angiogenesis, and metastasis by effects on tumor cells, endothelial cells, and pericytes in pancreatic cancer. Mol. Cancer Therapeut. *10*, 2157–2167. https://doi.org/10.1158/1535-7163.mct-11-0312.

Truong, D.D., Kratz, A., Park, J.G., Barrientos, E.S., Saini, H., Nguyen, T., Pockaj, B., Mouneimne, G., LaBaer, J., and Nikkhah, M. (2019). A human organotypic microfluidic tumor model permits investigation of the interplay between patient-derived fibroblasts and breast cancer cells. Cancer Res. *79*, 3139–3151. https://doi.org/10.1158/0008-5472.CAN-18-2293.

Votanopoulos, K.I., Forsythe, S., Sivakumar, H., Mazzocchi, A., Aleman, J., Miller, L., Levine, E., Triozzi, P., and Skardal, A. (2020). Model of patient-specific immune-enhanced organoids for immunotherapy screening: feasibility study. Ann. Surg Oncol. *27*, 1956–1967. https://doi.org/10.1245/s10434-019-08143-8.

Walker, C., Mojares, E., and del Río Hernández, A. (2018). Role of extracellular matrix in development and cancer progression. Int. J. Mol. Sci. *19*, 3028. https://doi.org/10.3390/ijms19103028.

Wang, S., Cao, C., Chen, Z., Bankaitis, V., Tzima, E., Sheibani, N., and Burridge, K. (2012). Pericytes regulate vascular basement membrane remodeling and govern neutrophil extravasation during inflammation. PLoS One *7*, e45499. https://doi.org/10.1371/journal.pone.0045499.

Wang, X., Ding, X., Nan, L., Wang, Y., Wang, J., Yan, Z., Zhang, W., Sun, J., Zhu, W., Ni, B., et al. (2015). Investigation of the roles of exosomes in colorectal cancer liver metastasis. Oncol. Rep. *33*, 2445–2453. https://doi.org/10.3892/or.2015.3843.

Xian, X., Hakansson, J., Stahlberg, A., Lindblom, P., Betsholtz, C., Gerhardt, H., and Semb, H. (2006). Pericytes limit tumor cell metastasis. J. Clin. Invest. *116*, 642–651. https://doi.org/10.1172/jci25705.

Yamada, T., Oshima, T., Yoshihara, K., Tamura, S., Kanazawa, A., Inagaki, D., Yamamoto, N., Sato, T., Fujii, S., Numata, K., et al. (2010). Overexpression of MMP-13 gene in colorectal cancer with liver metastasis. Anticancer Res. *30*, 2693–2699.

Yamaguchi, M., Hirai, S., Tanaka, Y., SUmi, T., Tada, M., Takahashi, H., Watanabe, A., and Sakuma, Y. (2020). Pericyte-myofibroblast transition in the human lung. Biochem. Biophys. Res. Commun. *528*, 269–275. https://doi.org/10.1016/j.bbrc.2020.05.091.

Yonenaga, Y., Mori, A., Onodera, H., Yasuda, S., Oe, H., Fujimoto, A., Tachibana, T., and Imamura, M. (2005). Absence of smooth muscle actin-positive pericyte coverage of tumor vessels correlates with hematogenous metastasis and prognosis of colorectal cancer patients. Oncology *69*, 159–166. https://doi.org/10.1159/000087840.

STAR★METHODS

KEY RESOURCES TABLE

REAGENT or RESOURCE	SOURCE	IDENTIFIER
Antibodies		
Mouse monoclonal anti-α-SMA	Abcam	Cat#ab7817, RRID: AB_262054
Donkey polyclonal anti-Mouse IgG	Thermo Fisher Scientific	Cat#A32744, RRID: AB_2762826
Paxillin monoclonal antibody, Mouse	Thermo Fisher Scientific	Cat#AHO0492, RRID: AB_2536312
Anti-Myosin light chain (phosphor S20) antibody, Rabbit	Abcam	Cat#ab2480, RRID: AB_303094
Chemicals, peptides, and recombinant proteins		
PhotoCol Methacrylated Collagen Type I	Advanced Biomatrix	Cat#5198
Heprasil Thiol-Modified Hyaluronin/Heparin	Advanced Biomatrix	Cat#GS215
Irgacure, 2-Hydroxy-4′-(2-hydroxyethoxy)-2-methylpropiophenone	Sigma Aldrich	Cat#410896
Alexa Fluor 488 Phalloidin	Thermo Fisher Scientific	A12379
MMP Biosensor Peptide	Leight et al. (2013)	N/A
Hoechst 33,342	Thermo Fisher Scientific	H1399
Critical commercial assays		
Sircol Soluble Collagen Assay	Biocolor Life Science Assays	S1000
Picro Sirius Red Stain Kit	Abcam	Ab150681
Human Simple-Step MMP-2 ELISA Kit	Abcam	Ab267813
Human Simple-Step MMP-9 ELISA Kit	Abcam	Ab246539
Human MMP-13 ELISA Kit	Abcam	Ab221839
Quantitative Proteomics Services: Human Cytokine Array 440	RayBiotech	QAH-CAA-440-1
Deposited data		
Quantitative proteomics raw data, all conditioned media types	This paper, RayBiotech	https://doi.org/10.17632/yjd5pbxdvm.1
Experimental models: Cell lines		
Human: Cell line Caco2	ATCC	HTB-37
Human: Cell line SW480	ATCC	CCL-228
Human: Cell line HCT116	ATCC	CCL-247
Human: Primary normal human lung fibroblasts	Lonza	CC-2512
Human: Primary human microvascular pericytes	ScienCell	Cat#1200
Software and algorithms		
ImageJ	Schneider et al. (2012)	https://imagej.nih.gov/ij/
R-Studio	R Studio Team (2020)	https://www.rstudio.com
CT-Fire	Bredfeldt et al. (2014a, 2014b)	https://eliceirilab.org/software/ctfire/
Other		
BlueWave RediCure 365 UV Lamp	Dymax	N/A

RESOURCE AVAILABILITY

Lead contact

Further information and requests for resources should be directed to and will be fulfilled by the lead contact, Aleksander Skardal (skardal.1@osu.edu).

Materials availability

This study did not generate new unique reagents.

Data and code availability

Conditioned media proteomic data have been deposited at Mendeley Data and are publicly available at https://doi.org/10.17632/yjd5pbxdvm.1 as of the date of publication of this manuscript. Accession numbers are listed below in the key resources table. All other data reported in this paper is available via the lead contact by request. This paper does not report original code. Any additional information required to reanalyze the data reported in this paper is available from the lead contact by request.

EXPERIMENTAL MODEL AND SUBJECT DETAILS

Cell lines

Caco2 (male, HTB-37, ATCC, Manassas, VA), SW480 (male, CCL-228, ATCC), and HCT116 (male, CCL-247, ATCC) were cultured in Dulbecco's Minimum Essential Medium (DMEM, Gibco) containing 10% fetal bovine serum (FBS, Gibco) and passaged with 0.05% Trypsin/EDTA at 70–90% confluency. Media was replenished every 3 days during culture.

Primary cell cultures

Normal human lung fibroblasts (NHLF CC-2512, Lonza, Morristown, NJ) and human microvascular pericytes (#1200, ScienCell, San Diego, CA) were expanded in tissue-culture treated plastic dishes. Cell cultures were passaged at 70–80% confluency, and all experiments were performed at or below the eighth passage. Fibroblasts were cultured in complete Fibroblast Growth Medium-2 BulletKit (Lonza) containing 2% FBS, and pericytes were cultured in complete Pericyte Medium (#1201, ScienCell) containing 2% FBS. Cells were detached from their plates with 0.05% Trypsin/EDTA (Gibco, Amarillo, TX) and resuspended their appropriate media for counting prior to use in hydrogel construct experiments. Media was replenished every 2 days for fibroblast and pericyte cultures. Sex of these cells cannot be reported due to donor variability for primary cell lots.

METHOD DETAILS

Conditioned media generation and proteomics

For all cell types, 1.5×10^6 cells were plated onto a 115 cm^2 tissue culture dish with 15 mL of their respective media and allowed to attach for 24 h. After this time, media was removed and replaced with either fibroblast or pericyte complete growth medium to generate conditioned fibroblast media and conditioned pericyte media. This conditioned media was gathered after 24 h to balance adequate cytokine content and nutrient depletion. Conditioned media were centrifuged for 10 min at 800 rcf to remove dead cells and large cell debris, and supernatants were aliquoted and frozen at −80 °C until use. Quantitative proteomic profiling was performed using testing services from RayBiotech (200 Human Proteins Q4000, RayBiotech, Inc., Norcross, GA). Heatmap representation of data was generated using RStudio open-source software.

Hydrogel construct fabrication

Fibroblasts or pericytes were suspended in hydrogel precursor solutions consisting of 3:1 methacrylated collagen I and thiolated hyaluronic acid. Briefly, thiolated hyaluronic acid (Advanced Biomatrix, Carlsbad, CA) was reconstituted at 1 mg/mL in sterile, degassed water containing 0.01% w/v photoinitiator (2-Hydroxy-4′-(2-hydroxyethoxy)-2-methylpropiophenone, Sigma, St. Louis, MO). Methacrylated collagen I (Advanced Biomatrix) was dissolved in sterile filtered 20 mM acetic acid to a final concentration of 6 mg/mL at 4 °C. Immediately before mixing hydrogel precursors, collagen I aliquots were neutralized with a sodium hydroxide neutralization solution (Advanced Biomatrix). The collagen and hyaluronic acid solutions were then combined at a 3:1 ratio and used to resuspend cells at 2,500 cells/μL. Cell-laden hydrogel precursors were pipetted in 10 μL droplets onto PDMS-coated 48-well plates and crosslinked with a 365 nm UV LED light (BlueWave RediCure 365, Dymax, Torrington, CT) for 2 s. The 10 μL hydrogels were cultured in 300 μL of conditioned media per well, with media aspirated and replenished daily to maintain nutrient supply.

Fluorescent staining

Hydrogel samples were fixed overnight in 4% paraformaldehyde at 4 °C, then washed 3 times with PBS (PBS) and stored in fresh PBS. Samples were permeabilized 10 min in 0.1% Triton X-100 (Sigma Aldrich, St. Louis, MO) and then blocked for 1 h in Blocker BSA 10X (Thermo Fisher Scientific, Waltham, MA) diluted to 1X in PBS. After washing, organoids were incubated overnight at 4 °C in a 1:200 dilution of anti-α-SMA (ab7817, Abcam, Cambridge, MA) in Cyto-Q ImmunoDiluent and Block (Innovex Biosciences, Richmond, CA), followed by a 1-h incubation with secondary antibody (Donkey anti-Mouse IgG Alexa Fluor Plus 594, Thermo Fisher Scientific) at 1:400 dilution. Counterstaining was performed with Alexa Fluor 488 phalloidin (A12379, Thermo Fisher Scientific) and Hoechst 33,342 (H1399, Thermo Fisher Scientific). Fluorescent images were taken with a Nikon A1R Confocal microscope (Nikon, Melville, NY).

Eccentricity measurements and calculation

Major and minor axes of fibroblasts and pericytes were measured from the phalloidin stain images taken in the previous section using ImageJ measurement tool. Measurements were made for all in-plane cells ($\geq$3 per image) in images from at least three replicates of each experimental condition. Eccentricity was calculated using the equation $\sqrt{1-\left(\frac{b^2}{a^2}\right)} = e^2$, where a is the semi-major axis, b the semi-minor axis, and e the eccentricity measure.

Matrix metalloproteinase ELISA

For matrix metalloproteinase (MMP) quantification, spent media was collected from fibroblast and pericyte hydrogel cultures on days 2 and 4 of conditioned media incubation. Samples were stored at −80 °C until use. To account for MMP presence in the conditioned media themselves, each conditioned media type was incubated at 37 °C in a cell culture incubator for 48 h, equal to the exposure time of media for each experimental sample. Secreted MMPs 2, 9, and 13 were quantified with the appropriate Human Matrix Metalloproteinase ELISA kits (ab267813, ab246539, ab221839, abcam). Absorbance measurements were read at 450 nm using a Varioskan LUX multimode plate reader (Thermo Fisher).

MMP peptide biosensor assays

Hydrogel constructs were synthesized as detailed above, with a 3:1 ratio of 6 mg/mL methacrylated collagen I:1 mg/mL thiolated HA. Prior to photocrosslinking, MMP-degradable biosensor peptide (Leight et al., 2013) was added to a final concentration of 25 μM and mixed thoroughly to ensure consistent distribution. Hydrogel precursor was then pipetted to form 10 μL droplets and crosslinked with 2 s of UV light. Fluorescence was immediately measured on a Varioskan LUX plate reader at 494 nm excitation/521 nm emission to establish baseline fluorescence of each construct. After adding the appropriate conditioned media, hydrogels were returned to a cell culture incubator and fluorescence measurements were repeated daily over a period of 8 days.

Soluble collagen quantification

Soluble (immature) collagen deposition in hydrogels was quantified using the Sircol Soluble Collagen Assay kit (Biocolor Life Science Assays, Carrikfergus, UK), following the manufacturer's protocol after 2 and 4 days of conditioned media culture, and on an acellular hydrogel construct directly after crosslinking as a negative control. Prior to performing the assay, hydrogels were treated with an acetic acid-pepsin digest as suggested by the manufacturer's protocol to release any newly-deposited collagen that had begun to form stable insoluble fibers. Absorbance was read at 555 nm.

Histological staining

After 3 and 7 days of conditioned media culture, hydrogel samples were fixed overnight in 4% paraformaldehyde at 4 °C, then washed 3 times with PBS and stored in fresh PBS. Fixed organoids were processed and embedded in paraffin, after which 6 μm sections were cut using a microtome (Leica Microsystems Inc., Buffalo Grove, IL) and mounted to slides. Slides were baked on a slide warmer for 1 h at 55 °C, followed by deparaffinization and rehydration.

For sections fixed after 3 days of conditioned media culture, immunofluorescent staining for phosphorylated myosin light chain and paxillin was performed following antigen retrieval with citrate buffer (ab93678, Abcam) and blocking in 4% Blocker BSA. Slides were incubated overnight at 4 °C in a 1:200

dilution of anti-myosin light chain (ab2480, Abcam) and anti-paxillin (AHO0492, Thermo Fisher Scientific) in 1% BSA, followed by a 1-h incubation with secondary antibodies (Goat anti-Rabbit IgG Alexa Fluor Plus 488, 1:200 dilution and Donkey anti-Mouse IgG Alexa Fluor Plus 594, 1:1000 dilution, Thermo Fisher Scientific). Counterstaining was performed with Hoechst 33,342 (H1399, Thermo Fisher Scientific). Fluorescent images were taken with a Nikon A1R Confocal microscope (Nikon, Melville, NY).

For sections fixed after 7 days of culture, Picrosirius Red (PSR) staining was performed with a commercially available staining kit (ab150681, Abcam) according to the manufacturer's staining protocol. Brightfield birefringence imaging was performed using a Nikon TI2-E microscope and NIS-Elements AR v5.20 software. Circular polarizing films (Edmund Optics, Barrington, NJ) were aligned on each side of the specimen, allowing only signal from collagen birefringence to be transmitted. Images were taken for ≥ 3 samples in each condition, with one region of interest quantified for each sample.

Collagen fiber quantification and analysis

PSR signal was quantified through fiber segmentation using the CT-FIRE program (Laboratory for Optical and Computation Instrumentation, University of Wisconsin) (Bredfeldt et al., 2014a, 2014b). Birefringence images were selected where hydrogels covered the entire field of view and converted to grayscale using ImageJ (Schneider et al., 2012). CT-FIRE processing was applied to the set of images in parallel, and results from sample groups were compiled. All graphs represent pooled results from $n \geq 3$ images, representing 1000–5000 fibers each. Fiber angles are shown as difference from the median angle from each individual image dataset to account for differences in slide orientation.

QUANTIFICATION AND STATISTICAL ANALYSIS

Statistical analysis

All experiments above were performed with n = 3 unless otherwise specified. Statistical analysis was performed using GraphPad Prism software v9.2.0 (GraphPad Software, La Jolla, CA). Parametric data was analyzed using a one-way ANOVA with subsequent Tukey's multiple comparisons tests. Non-parametric data was analyzed using the Kruskal-Wallis test with subsequent Dunn's multiple comparisons tests. For all tests, a statistically significant difference was considered to be a p value less than or equal to 0.05, and p values are reported as (*$p < 0.05$), (**$p < 0.01$), (***$p < 0.001$), (****$p < 0.0001$). Statistical details for each experiment can be found in the appropriate figure legend.